International Journal of Environmental Science and Technology (2019) 16:5741–5756
https://doi.org/10.1007/s13762-018-1941-2

ORIGINAL PAPER

A designed experimental approach for photocatalytic degradation of paraquat using α-Fe_2O_3@MIL-101(Cr)@TiO_2 based on metal–organic framework

A. Khodkar[1] · S. M. Khezri[2] · A. R. Pendashteh[3,4] · S. Khoramnejadian[1] · L. Mamani[2]

Received: 29 December 2017 / Revised: 22 July 2018 / Accepted: 31 July 2018 / Published online: 10 August 2018
© Islamic Azad University (IAU) 2018

Abstract

A new magnetic α-Fe_2O_3@MIL-101(Cr)@TiO_2 photocatalyst was successfully prepared. The structural and morphological properties of synthesized photocatalyst were studied by FTIR, XRD, SEM, EDX and BET analysis. Optimizing of the removal of paraquat herbicide from aqueous solution was investigated by response surface methodology based on Box–Behnken design. The interactive effects of four parameters including the dosage of catalyst, pH, the initial concentration of paraquat and contact time, all have been studied on the photocatalytic degradation and COD reduction. A quadratic polynomial model was adjusted to the data with an R^2 of 0.89 for photocatalytic degradation and R^2 of 0.92 for COD reduction, respectively. The photocatalytic degradation and COD reduction were obtained 87.46% and 90.09% at the optimal conditions, after 45 min using 0.2 g L^{-1} of α-Fe_2O_3@MIL-101(Cr)@TiO_2, pH 7 and the concentration of paraquat 20 mg L^{-1}. The kinetics of paraquat adsorption on the surface of α-Fe_2O_3@MIL-101(Cr)@TiO_2 photocatalyst were obtained by the pseudo-second-order and parabolic diffusion models.

Keywords Paraquat · Box–Behnken design · Photodegradation · Chemical oxygen demand

Introduction

Nowadays, water contamination is the main environmental problem that can be generated by organic pollutants containing herbicides, pesticides, pharmaceuticals and care products (Gobas et al. 1993). These compounds have toxic and non-biodegradable properties. They usually can be stored in the body as well. In order to maintain the quality and quantity of crops production, a wide range of pesticides are applied in horticulture and agriculture. Pesticides are involved fungicide, nematicide, herbicide, acaricide, insecticides, etc (Marien et al. 2016). These compounds are persistent and highly stable due to the formation of their organic complex. Using the pesticides leads to the serious dangers on the health of human. Therefore, the removal of these compounds must be considered significantly (Ahmed et al. 2011).

Paraquat dichloride or paraquat (1,1-dimethyl-4,4′-bipyridylium dichloride) is one of the most important herbicides for controlling the weeds in agricultural products (De-Almeida and Yonamine 2007). This non-selective herbicide has significant properties such as high toxic effects, significant binding potential and notable solubility in the water. Paraquat can cause serious hazards for the environment and human health (Dhaouadi and Adhoum 2009). So, the removal or degradation of paraquat dichloride from water is an essential factor to prevent environmental pollution. The development of effective systems for the removal of organic contaminants from water stands as an essential need.

In recent years, removal of different types of pesticides has been reported using various methods like coagulation–flocculation (Saini and Kumar 2016; Shabeer et al. 2014), membrane separation (Doulia et al. 2016; Plakas

---

Editorial responsibility: Dr. J Aravind, M.Tech, Ph.D.

✉ S. M. Khezri
khezri34@gmail.com

[1] Department of the Environment, Damavand Branch, Islamic Azad University, Damavand, Iran

[2] Faculty of Environment and Energy, Tehran Science and Research Branch, Islamic Azad University, Tehran, Iran

[3] The Caspian Sea Basin Research Center, University of Guilan, Rasht, Iran

[4] Department of Chemical Engineering, University of Guilan, Rasht, Iran

and Karabelas 2012), adsorption (Bajuk-Bogdanovic et al. 2017; Liu et al. 2017), bioremediation (Alvarez et al. 2016; Castillo Diaz et al. 2016) and advanced oxidation processes (AOPs) (Marien et al. 2016). AOPs can fully mineralize the organic contaminates through the generation of highly oxidizing species such as superoxide or hydroxyl radicals. These methods are effective due to the low cost, high efficiency and their environmental-friendly state (Marien et al. 2016). Moreover, this method can be involved in the processes such as ultrasound, electro-Fenton, ozonolysis and oxidation with H_2O_2 under UV irradiation (Petit et al. 1995; Reddy and Kim 2015; Real et al. 2007; Kida et al. 2018; Zhang et al. 2010).

Among advanced oxidation processes, photocatalysis has attracted attentions as a favorable substituted method in the comparison with traditional wastewater treatment. This reaction is a non-selective process that can directly convert the contaminants into the harmless materials (Daneshvar et al. 2007).

Up to date, the photodegradation of organic compounds was performed by semiconductor photocatalysts including, ZnO, CdS, TiO_2, WO_3, etc (Lin et al. 2005; Kown et al. 2000; Liu et al. 1998). Among the different types of photocatalysts, titanium dioxide (TiO_2) is mostly used as semiconductors for the removal of organic compounds because of its high efficiency, low cost, non-toxic nature, photochemical stability and commercial availability (Roy et al. 2011; Chen and Mao 2007). Usually, titanium dioxide generates electron–hole pairs under UV light in photocatalytic degradation of organic pollutants. The hydroxyl and superoxide radicals are generated after separation. These radicals can oxidize the organic pollutants. The hydroxyl radicals are produced by the reaction of the holes with water molecule or adsorbed hydroxyl anion. Superoxide radicals are formed via the reaction of electrons with dissolved dioxygen (Marien et al. 2016).

One of the problems of titanium dioxide nanoparticles is difficult separation from the treated water (Wang et al. 2011; Xi et al. 2011). Sedimentation is a common method for separation of TiO_2 photocatalyst. This method is a time-consuming process; furthermore, a part of TiO_2 still remains in the treated water (Guo et al. 2011). Hence, the combination of TiO_2 nanoparticle and magnetic nanomaterials (such as Fe_3O_4 and Fe_2O_3) has recently become an important topic of research in preparation of TiO_2 photocatalysts (Beydoun et al. 2000; Lee et al. 2004; Makovec et al. 2011). Among different nanomaterials, metal–organic frameworks (MOFs) are the field of interest over the past two decades. The porous crystalline materials are made of metal ions like zinc, copper, chromium, aluminum, zirconium which are coordinated with organic ligands (Wee et al. 2014). These compounds have unique properties such as high surface area, easy separation, high porosity, and diversity of functions and structures (E-Shall et al. 2009). They can be used in different fields including gas storage (Zhao et al. 2011), drug delivery (Horcajada et al. 2008, 2011; Taylor-Pashow et al. 2009), catalysis (Nguyen et al. 2017; Corma et al. 2010) and selective adsorption as well as separation (Li et al. 2009).

Up to now, the synthesis of magnetic photocatalyst based on the metal–organic framework (Dekrafft et al. 2012) and TiO_2-based magnetic photocatalysts (Chen et al. 2011; Su et al. 2016; Mirmasoomi et al. 2016) have been reported in the literature which is an interesting subject. However, there are only few reports for removal of paraquat using photocatalytic processes such as UV/$ZrTiO_4$/$ZrTi_2O_6$/TiO_2 (Nur-Afiqah et al. 2016), Cu-TiO_2/SBA-15 (Sorolla et al. 2012), UV/TiO_2 (Moctezuma et al. 1999; Florencio et al. 2004; Nagaraju et al. 2017), or TiO_2 immobilized films (Tennakone and Kottegoda 1996; Noguchi et al. 1998; Lei et al. 1999; Kang 2002; Zahedi et al. 2015), or UV-ozonation method (Kearney et al. 1985), electrochemical advanced oxidation methods (electro-Fenton and photoelectro-Fenton) (Dhaouadi and Adhoum 2009) and photo-Fenton process (Trovo et al. 2013).

In this study, a novel magnetic α-Fe_2O_3@MIL-101(Cr)@TiO_2 photocatalyst was successfully prepared and its photocatalytic activity was tested on the degradation of paraquat in aqueous solution. The effective parameters such as contact time, pH, catalyst dosage and concentration of herbicide were optimized by response surface methodology (RSM) based on central composite design (CCD).

Materials and methods

Materials and instrumentation

All reagents were of an analytical grade and were used without further purification. The terephthalic acid (H_2BDC), chromium(III) nitrate nonahydrate ($Cr(NO_3)_3 \cdot 9H_2O$), iron(III) chloride hexahydrate ($FeCl_3 \cdot 6H_2O$), iron(II) chloride tetrahydrate ($FeCl_2 \cdot 4H_2O$), tetra butyl ortho titanate (TBOT), paraquat (purity = 95–98%), sodium hydroxide (NaOH), ammonia solution ($NH_3 \cdot H_2O$, 30%), hydrchloric acid, acetic acid, deionized water and ethanol (96%) were purchased with high purity from Fluka, Merck and Sigma-Aldrich chemical companies. The terephthalic acid (H_2BDC) and chromium(III) nitrate nonahydrate ($Cr(NO_3)_3 \cdot 9H_2O$) are used as a reagent for the synthesis of MIL-101(Cr). The iron(III) chloride hexahydrate ($FeCl_3 \cdot 6H_2O$) and iron(II) chloride tetrahydrate ($FeCl_2 \cdot 4H_2O$) are applied as reagents and NaOH as a catalyst for the synthesis of the Fe_2O_3 nanoparticle. The tetra butyl ortho titanate (TBOT) is used for the synthesis of TiO_2 on the surface of Fe_2O_3 @MIL-101(Cr). In the synthesis of Fe_2O_3@MIL-101(Cr)@TiO_2, the pH value was adjusted by adding hydrchloric acid, acetic acid and sodium hydroxide. The composition and structure of synthesized photocatalyst were characterized by a Fourier transform infrared (Shimadzu, FTIR-8900) spectrometer. The crystallinity and crystal phases of photocatalyst were measured by X-ray diffraction (PHILIPS PW1730) with Cu-Ka radiation in the range of (XRD normal) 10–80 (2θ) and (low-angle XRD) 0–10 (2θ). Scanning electron microscopy (TE-SCAN) at 15 kV equipped with an energy-dispersive X-ray spectrometer was used for determination of morphology and size of the prepared photocatalyst. X-ray energy-dispersive spectroscopy (EDX) was used to determine the chemical composition and the elements. Pore size distribution was analyzed using desorption branch of the isotherm through the Barrett–Joyner–Halenda (BJH) method, and specific surface areas were calculated by the Brunauer–Emmett–Teller (BET) method. The nitrogen adsorption–desorption isotherms obtained at 77 K on BELSORP-mini II, (BEL-Japan). In this study, a light source with 125 W medium-pressure UVC lamp (Arda, France) and emitting maximum wavelength at 247.3 nm was applied (Shokofan Tosee Company, Iran).

Preparation of (α-Fe_2O_3 @MIL-101(Cr)@TiO_2)

The magnetic α-Fe_2O_3@MIL-101(Cr)@TiO_2 photocatalyst was prepared in three steps. Firstly, MIL-101(Cr) was synthesized hydrothermally according to the method reported in the literature (Bhattacharjee and Chena Ahn 2014). A mixture of terephthalic acid (H_2BDC) (0.332 g, 2 mmol), chromium(III) nitrate nonahydrate ($Cr(NO_3)_3 \cdot 9H_2O$) (0.8 g, 2 mmol) and sodium hydroxide (NaOH) (0.2 g, 5 mmol) were added to 10 mL deionized water (DW) in a 50-mL magnetically stirred glass vial. The sample was heated at 160 °C for 16 h and then was slowly cooled down to atmospheric temperature. The green suspension of MIL-101 was filtered and centrifuged at 3000 rpm (for 15 min to collect the first precipitates of MIL-101) and 4000 rpm (for 15 min to collect the second precipitates of MIL-101). The second precipitates of MIL-101 were washed with deionized water (2 × 20 mL), ethanol (96%) (2 × 20 mL) and dried at 80 ◦C for 24 h in a hot air oven.

At the second step, magnetic Fe_2O_3@MIL-101(Cr) nanoparticle was synthesized via a co-precipitation method (Sajjadifar et al. 2014). In this synthesis, (0.198 g, 1 mmol) of $FeCl_2.4H_2O$, (0.540 g, 2 mmol) of $FeCl_3.6H_2O$ and 30 mL of deionized water were added to an aqueous suspension (10 mL) containing 0.5 g of MIL-101(Cr). The mixture was stirred at room temperature for 1 h. Then, an ($NH_3 \cdot H_2O$, 30%) solution (15 mL) was dropped into the mixed solution until the pH value reached 10 and a large amount of black precipitates were produced. After 2 h of heating at 80 °C, black solids were slowly cooled down to room temperature. The resulting black solids were recovered by magnetic separation and repeatedly washed with deionized water until the pH became neutral. The dark brown precipitates formed were washed with ethanol (96%) (2 × 20 mL) and dried at 80 °C for 24 h in a hot air oven to give Y or α-Fe_2O_3@MIL-101(Cr). However, the Fe_3O_4 was transformed to Fe_2O_3 (α-Fe_2O_3 and γ-Fe_2O_3 phases) that was proved by XRD measurement (Fig. 2).

Finally, the magnetic α-Fe_2O_3@MIL-101(Cr)@TiO_2 photocatalyst was synthesized via sol–gel technology. The α-Fe_2O_3@MIL-101(Cr) nanoparticle (0.5 g) was dispersed in the mixture solution of water–ethanol with a volume ratio of 1:20. Then, the mixture was sonicated for 20 min in a powerful ultrasonic apparatus (sound intensity of 80 W cm^{-2}). A dilute hydrochloric acid aqueous solution was added to the suspension until the pH value of the mixture was 4–5. A mixture solution of 7.5 mL tetrabutyl orthotitanate (TBOT) in 20 ml ethanol (96%) and 4 mL acetic acid (10%) prepared under magnetic stirring in 10 min. Then, this mixture was slowly dropped into the above suspension. The suspension was heated at 80 °C for 15 min. The precipitates were recovered by magnetic separation and washed with deionized water (2 × 20 mL) and ethanol (96%) (2 × 20 mL) until the pH became about 7. The magnetic photocatalyst particles were dried in an oven at 80 °C and calcined at 500 °C for 2 h.

Photocatalytic degradation experiments

A stock solution (1000 mg L^{-1}) of paraquat was prepared by dissolving paraquat in distilled water in order to investigate the efficiency of degradation. A certain dosage of the photocatalyst (0.1–0.5 g L^{-1}) was poured in 1 L of paraquat solution with pH (3–11) and different concentrations (10–50 mg L^{-1}) in each experiment. The pH of each solution was adjusted by adding NaOH or HCl (0.1 mol L^{-1}) and measured by pH meter (Metron, Switzerland). All reactions were performed at constant temperature (25 ± 1 °C) for 15–75 min. Each solution was kept in the dark for 30 min for adsorption–desorption equilibrium. Then, the UV lamp was placed above the solution with 10 cm distance. After completion of reaction time, the suspension was centrifuged (Sigma-301, Germany) at 4000 rpm for 15 min for separation of nanocatalyst. The changes in the paraquat concentration were evaluated using a double beam UV–Vis spectrophotometer (Perkin–Elmer–Lambda 25, USA) at $\lambda_{max} = 257$ nm with a calibration curve based on Beer–Lambert law (Horwitz 2000). The efficiency of photocatalytic degradation of paraquat was evaluated according to the equation:

$$\text{Phtocatalytic degradation (\%)} = \frac{C_o - C}{C_o} \times 100 \tag{1}$$

In Eq. 1, C_o is the initial concentration (g L^{-1}) and C is the final concentration (g L^{-1}) after photocatalytic degradation of paraquat.

COD reduction analysis

The COD analysis was used for determining the amount of organic compounds in samples before and after the photocatalytic reaction. In the present study, potassium dichromate analysis was utilized for measuring COD (American Public Health Association, APHA 2005). The percentage of COD reduction was computed using the following equation:

$$\text{COD reduction }(\%) = \frac{(\text{COD}_o - \text{COD})}{\text{COD}_o} \times 100 \quad (2)$$

In Eq. 2, COD_o and COD are the evaluated COD values before and after the photocatalytic reaction, respectively.

Design of experiments and statistical analysis

In this study, a response surface methodology (RSM) based on Box–Behnken design (BBD) was employed in order to reduce the number of experiments. The number of experiments were obtained 29. RSM is a significant, fast and economical statistics technique for the determination of interactive effects of parameters on experimental data (Fu et al. 2009). The variables and their levels selected for the photocatalytic degradation of paraquat were catalyst dosage (0.2–0.4 g L^{-1}), the paraquat concentration (20–40 mg L^{-1}), reaction time (30–60 min) and pH (3–11) (Table 1). Photocatalytic degradation and COD reduction were evaluated as the responses shown in Table 2. In this study, a software package of Design Expert version 7.0.0 (Stat-Ease, Statistics Made Easy, Minneapolis, MN, USA) was applied. The models were studied from linear to partial cubic state, and a quadratic polynomial model was obtained suitable for investigating the effects of parameters. An analysis of variance (ANOVA) was applied to adequate the developed models with the observed data.

Results and discussion

Characterization of α-Fe_2O_3@MIL-101(Cr)@TiO_2

Fourier transform infrared analysis of catalyst

The FTIR spectra of the MIL-101(Cr), α-Fe_2O_3@MIL-101(Cr) and α-Fe_2O_3@MIL-101(Cr)@TiO_2 are shown in Fig. 1. The FTIR spectrum of MIL-101(Cr) (Fig. 1) is similar to the previous results (Jhung et al. 2007). The strong bands at 1562 and 1384 cm^{-1} can be assigned to the vibrational stretching frequencies of the framework (O–C–O), confirming the presence of dicarboxylate linker in the MIL-101 framework (Jhung et al. 2007). The bands between 1430 and 1550 cm^{-1} are attributed to the stretching vibration (C=C) of benzene. The vibrations of benzene rings (C–H) were observed at 1097, 1020, 825 and 744 cm^{-1} (Maksimchuk et al. 2008). The bands at about 509 cm^{-1} are most likely to ascribe to in-plane and out-of-plane bending modes of (COO^-) groups (Maksimchuk et al. 2008). The band at 3429 cm^{-1} is due to the water molecules within the pores of MIL-101(Cr).

The FTIR spectrum of Fe_2O_3@MIL-101(Cr) is presented in (Fig. 1). The bands at around 3427 and 1627 cm^{-1} can be assigned to the (–OH) stretching modes and bending vibration of the free or adsorbed water. In addition, the characteristic absorption band of 524, 576 cm^{-1} was associated with (Fe–O) bonds. The (C=C) stretching vibrations of benzene ring occurred in the range of 1430–1550 cm^{-1}. The reduction of intensity can be attributed to the generation of Fe_2O_3 on MIL-101(Cr). The expand band at 931 cm^{-1} was attributed to the out-of-plane bending vibration of (C–H) bonds. Also, the stretching of (C=C) bonds appeared at 524–750 cm^{-1} overlapped with (Fe–O) bending modes.

The FTIR spectra of Fe_2O_3@MIL-101(Cr)@TiO_2 refer to the successful formation of this compound (Fig. 1). All bands of MIL-101(Cr) and Fe_2O_3@MIL-101(Cr) appeared in their place. The spectrum showed a relatively broad band in the range of 3200 to 3520 and 1625 cm^{-1}, which indicated the presence of the (–OH) group of the free or adsorbed water molecules. The bands around 1423 and 1535 cm^{-1} of (O–C–O) groups confirm the presence of the dicarboxylate moieties within MIL-101. Also, the stretching of (C=C) bonds in benzene ring observed in the region 1430–1550 cm^{-1} overlapped with (O–C–O) groups.

The presented bands of 800–950 and 1041 cm^{-1} correspond to the (Ti–O–C) stretching vibrations (Cheng et al. 2004). The (Ti–O–C) bond is predicted to be the result of an interaction between the (Ti–O) network and the (C=O) from dicarboxylate linker in the MIL-101 framework. The broadband centered at 550–700 cm^{-1} was likely due to the vibration of the (Ti-O-Ti) bonds in the TiO_2 lattice that overlapped with the stretching vibration of (C=C)

Table 1 Crystallographic data obtained from XRD of α-Fe_2O_3@MIL-101(Cr)@TiO_2

Entry	Phases present	2θ°	Crystal system	Lattice parameters (Å)			D^a_{XRD} (nm)
				a	*b*	*c*	
1	α-Fe_2O_3	35.65	Rhombohedral	5.0342	5.0342	13.7483	32.8
2	TiO_2	25.29	Tetragonal	3.7892	3.7892	9.5370	36.2
3	TiO_2	48.04	Tetragonal	3.8040	3.8040	9.6140	77.4

[a] The mean crystal size

Table 2 Composition of various experiments of the Box–Behnken design, and photocatalytic degradation and COD reduction responses for paraquat removal and ANOVA analysis of the quadratic polynomial model

Exp. no.	Variable				Photocatalytic degradation (%)	COD reduction (%)
	A: catalyst dosage (g L^{-1})	*B*: paraquat concentration (mg L^{-1})	*C*: pH	*D*: contact time (min)		
1	0.20	20.00	7.00	45.00	87.46	90.09
2	0.40	20.00	7.00	45.00	64.58	72.69
3	0.20	40.00	7.00	45.00	29.45	55.8
4	0.40	40.00	7.00	45.00	32.96	54.97
5	0.30	30.00	5.00	30.00	38.88	61.53
6	0.30	30.00	9.00	30.00	39.25	61.06
7	0.30	30.00	5.00	60.00	39.82	55.42
8	0.30	30.00	9.00	60.00	40.49	65.75
9	0.20	30.00	7.00	30.00	39.25	75.15
10	0.40	30.00	7.00	30.00	29.86	68.5
11	0.20	30.00	7.00	60.00	40.49	69.98
12	0.40	30.00	7.00	60.00	32.12	69.04
13	0.30	20.00	5.00	45.00	47.1	71.67
14	0.30	40.00	5.00	45.00	31.78	44.15
15	0.30	20.00	9.00	45.00	55.29	70.68
16	0.30	40.00	9.00	45.00	31.8	44.62
17	0.20	30.00	5.00	45.00	36.09	63.87
18	0.40	30.00	5.00	45.00	31.67	69.04
19	0.20	30.00	9.00	45.00	38.49	69.51
20	0.40	30.00	9.00	45.00	31.92	70.45
21	0.30	20.00	7.00	30.00	70.99	88.88
22	0.30	40.00	7.00	30.00	30.38	57.56
23	0.30	20.00	7.00	60.00	69.6	70.18
24	0.30	40.00	7.00	60.00	31.32	53.32
25	0.30	30.00	7.00	45.00	58.12	78.15
26	0.30	30.00	7.00	45.00	57.56	76.56
27	0.30	30.00	7.00	45.00	57.23	79.37
28	0.30	30.00	7.00	45.00	55.89	79.84
29	0.30	30.00	7.00	45.00	56.1	78.44

Source	Sum of squares	Degree of freedom	Mean square	*F* value	*p* value
Model for photodegradation	5784.14	8	723.02	21.03	< 0.0001
A—Catalyst dosage	192.96	1	192.96	5.61	0.0280
B—Paraquat concentration	3582.14	1	3582.14	104.18	< 0.0001
C—Ph	11.80	1	11.80	0.34	0.5645
D—Time	2.28	1	2.28	0.066	0.7994
AB	174.11	1	174.11	5.06	0.0358
A^2	617.71	1	617.71	17.97	0.0004
C^2	1235.58	1	1235.58	35.94	< 0.0001
D^2	493.93	1	493.93	14.37	0.0011
Residual	687.67	20	34.38		
Lack of fit	684.01	16	42.75	46.71	0.0010
Pure error	3.66	4	0.92		
Corrected total	6471.80	28			
Model for COD reduction	3339.08	9	371.01	25.12	< 0.0001
A—Catalyst dosage	32.37	1	32.37	2.19	0.1551
B—Paraquat concentration	1970.43	1	1970.43	133.43	< 0.0001

Table 2 (continued)

Source	Sum of squares	Degree of freedom	Mean square	*F* value	*p* value
C—pH	22.39	1	22.39	1.52	0.2333
D—Time	70.04	1	70.04	4.74	0.0422
AB	68.64	1	68.64	4.65	0.0441
BD	52.27	1	52.27	3.54	0.0753
B^2	405.75	1	405.75	27.48	<0.0001
C^2	832.41	1	832.41	56.37	<0.0001
D^2	171.31	1	171.31	11.60	0.0030
Residual	280.58	19	14.77		
Lack of fit	274.14	15	18.28	11.35	0.0152
Pure error	6.44	4	1.61		
Corrected total	3619.67	28			

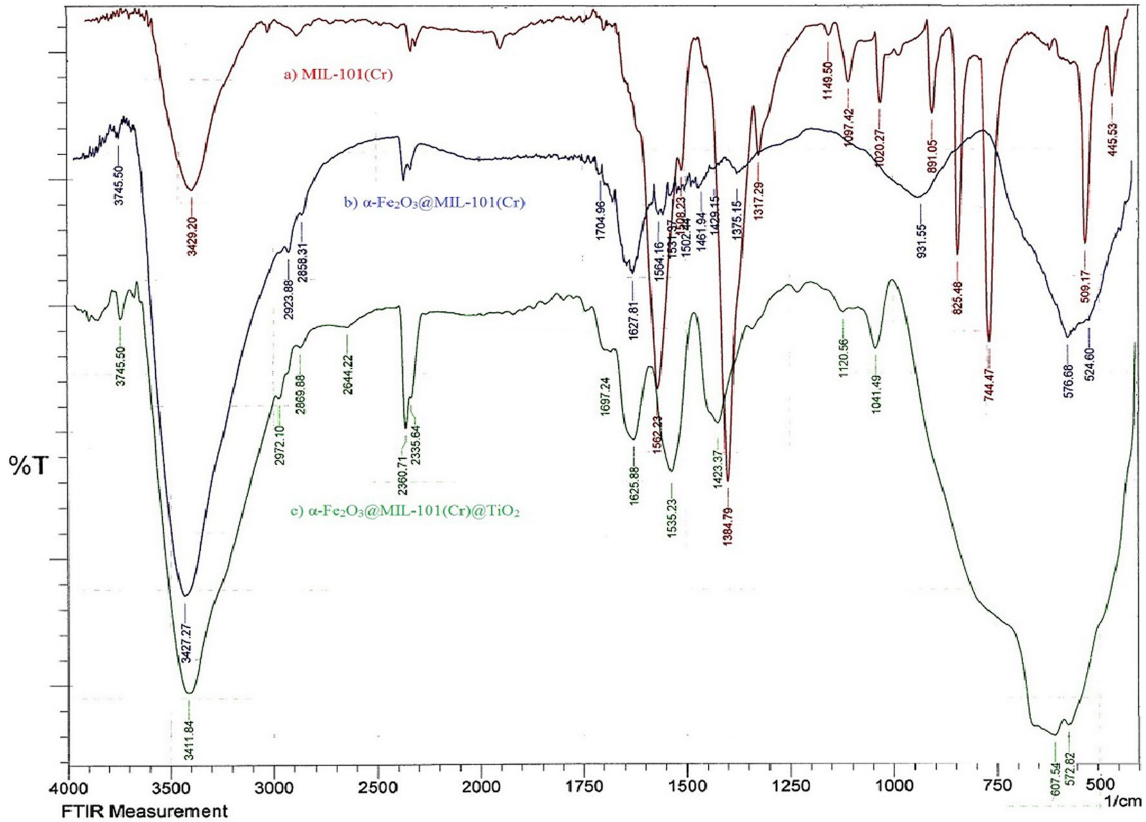

Fig. 1 FTIR spectra of the MIL-101(Cr), α-Fe_2O_3@MIL-101(Cr) and α-Fe_2O_3@MIL-101(Cr)@TiO_2

and (Fe–O) bonds from Fe_2O_3. These data reveal that the novel Fe_2O_3@MIL-101(Cr)@TiO_2 magnetic photocatalyst was constructed.

XRD analysis of α-Fe_2O_3@MIL-101(Cr)@TiO_2

The crystalline nature of magnetic α-Fe_2O_3@MIL-101(Cr)@TiO_2 photocatalyst was confirmed by normal and low-angle XRD analysis, merged in Fig. 2. The low-angle XRD patterns of α-Fe_2O_3@MIL-101(Cr)@TiO_2 together with the pattern of parent MIL-101(Cr) are characteristic of MIL-101(Cr) (Xu et al. 2015). The formation of the MIL-101(Cr) was investigated by the small angle XRD ($2\theta = 2°–10°$). The diffraction peaks of the MIL-101(Cr) at $2\theta = 5.1°$, 5.5° and 9.8° are related to (115), (135) and (119) as reported previously (Cheng et al. 2004; Xu et al. 2015). Diffraction peaks at around $2\theta = 24.1°$, 33.1°, 35.6°, 40.8°, 56.1°, 64.0° and 72.3° are related to (012), (104), (110), (113), (116), (214) and (300) which are easily recognized through the XRD analysis. The observed diffraction peaks agree well with the rhombohedral structure of α-Fe_2O_3 (JCPDS cards 33-0664). The results show that the crystal formation of hematite phase started at 500 °C.

The diffraction peaks at $2\theta = 25.2°$, 36.8°, 37.6°, 38.5°, 48.0°, 53.7°, 54.9°, 62.5° and 74.8° were related to (101), (103), (112), (004), (112), (200), (105), (211), (204) and (215) orientation planes of anatase TiO_2 with the tetragonal structure (JCPDS card No 71-1119). The prominent peak at angle 25.2° was illustrated the anatase phase as the major phase, while a small peak at angle 35.6° indicated the presence of α-Fe_2O_3. Based on Scherer's equation, the mean crystal size of the α-Fe_2O_3 and TiO_2 films was achieved 32.8 and 36.2 nm, respectively (Table 1).

$$D = \frac{K\lambda}{\beta\cos\theta} \tag{3}$$

where D is the mean crystal size, K a dimensionless shape factor with a value close to unity (0.94), λ the X-ray wavelength, β the line broadening at half the maximum intensity (FWHM), and θ is the Bragg angle.

Nitrogen adsorption–desorption analysis of α-Fe_2O_3@MIL-101(Cr)@TiO_2

The nitrogen adsorption–desorption isotherms of α-Fe_2O_3@MIL-101(Cr)@TiO_2 photocatalyst are shown in Fig. 3a. The BET surface area of the catalyst is 67.58 $m^2\ g^{-1}$. Significantly, the specific surface area is much higher than previously reported value (11.6 $m^2\ g^{-1}$) of α-Fe_2O_3@TiO_2@MIL-101 (Dekrafft et al. 2012). This result combined with the SEM and EDX images and reveals that α-Fe_2O_3@TiO_2 structure has a metal–organic framework. The isotherms are identified as type IV, according to the IUPAC classification (Cheng et al. 2004) that are the characteristic isotherm of mesoporous materials. The total pore volume of at $P/P_0 = 0.990$ is 0.1779 $cm^3\ g^{-1}$. However, the curve exhibits a loose mesoporous structure at high relative pressures between 0.8 and 1.0. The pore size distribution data are indicated in 4.65 nm (Fig. 3b).

Field emission scanning electron microscopy analysis of α-Fe_2O_3@MIL-101(Cr)@TiO_2

The field emission scanning electron microscopy (FESEM) was used to determine the morphology of α-Fe_2O_3@MIL-101(Cr)@TiO_2 photocatalyst. The spherical and uniform spherical-shape structure in the synthesized catalyst is shown in Fig. 4a. Also, the spherical area is rough that reveals crystalline nature of titania shell, nucleation and growth process of TiO_2 on the surface of α-Fe_2O_3 cores. These figures show the distribution of TiO_2 particles on Fe_2O_3 with the mean diameter of 14–27 nm.

Energy-dispersive X-ray analysis of α-Fe_2O_3@MIL-101(Cr)@TiO_2

The energy-dispersive X-ray spectroscopy (EDX) was applied to illustrate the elemental distribution in α-Fe_2O_3@

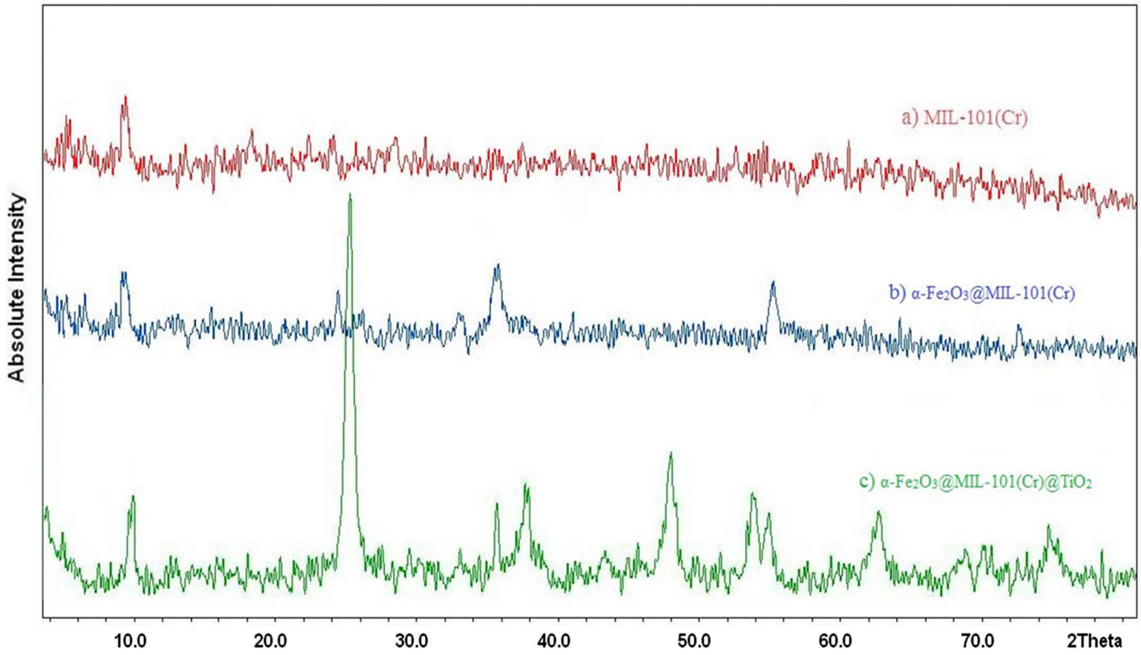

Fig. 2 The XRD pattern of the **a** MIL-101(Cr), **b** α-Fe_2O_3@MIL-101(Cr) and **c** α-Fe_2O_3@MIL-101(Cr)@TiO_2

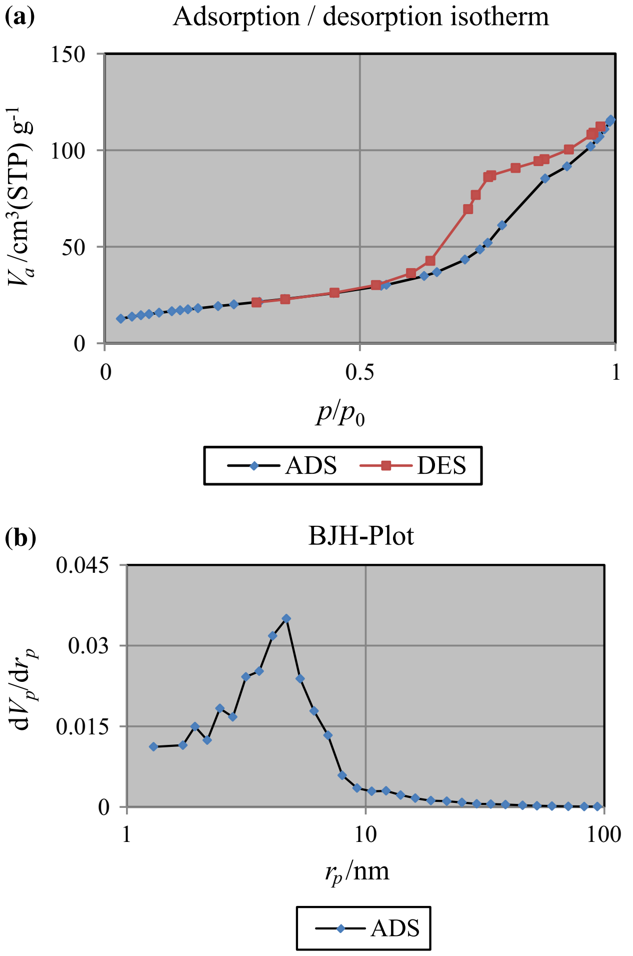

Fig. 3 **a** Nitrogen adsorption–desorption isotherms (ADS-DES) at 77 K for the α-Fe_2O_3@MIL-101(Cr)@TiO_2. **b** Pore size distribution isotherm at 77 K for the α-Fe_2O_3@MIL-101(Cr)@TiO_2

MIL-101 (Cr)@TiO_2 photocatalyst. The peaks of Cr, Fe, Ti and O elements with element contents of 2.33%, 6.31%, 29.32% and 62.04% (by weight), respectively, are shown in Fig. 4b. The higher peak intensity of Ti with respect to that of Fe is due to the higher fraction of TiO_2 in photocatalyst and its shielding effect. Moreover, the presence of the Cr peak is also attributed to the formation of MIL-101 in photocatalyst.

Model fitting and ANOVA

Photocatalytic degradation

The obtained photocatalytic degradation percentages using design matrix of the variables are given in Table 2. Fitting of the data to various models including linear, two factorial, quadratic, and cubic was investigated with their subsequent ANOVA. The results showed that a quadratic polynomial model was the most suitable one for photocatalytic degradation reaction. The equation of the model in terms of coded factors is described by the following equation:

$$\begin{aligned}\text{Photocatalytic degradation }(\%) &= 58.15 - 4.01A \\ &- 17.28B + 0.99C + 0.44D + 6.60AB - 9.58A^2 \\ &- 13.55C^2 - 8.57D^2\end{aligned} \tag{4}$$

where A is the catalyst dosage (g L^{-1}), B paraquat concentration (mg L^{-1}), C pH, and D the contact time (min). The ANOVA analysis for this model is shown in Table 2. The insignificant terms were omitted from the model. The F value of the model (21.03) with a p value less than 0.05 (<0.0001) was obtained that showed this model is significant at the 95% confidence level. Also, a high coefficient of determination ($R^2=0.8937$) is achieved. Adequate precision measured as a signal-to-noise ratio for the developed model (15.34) was greater than 4. This amount indicated that the model could be applied to navigate the design space as well. The results showed that this model is convenient for demonstrating the real relationship among the parameters. The importance of each term in the model was studied by testing the null hypothesis. The catalyst dosage and paraquat concentration had significant effects on the photocatalytic degradation, while pH and the contact times were not important factors. Also, in this model AB, A^2, C^2 and D^2 were the remarkable model terms.

COD reduction

Moreover, the effect of parameters on the COD reduction is considered using Box–Behnken design (BBD). The obtained COD reduction percentages using design matrix of the parameters are shown in Table 2. The results showed that a quadratic polynomial is the most significant model for COD reduction with a very small p value (<0.0001), F value (25.12) and a high coefficient of determination ($R^2=0.9225$). Adequate precision measured as a signal-to-noise ratio of the developed model (19.45) (>4) that indicated the model could be applied to navigate the design space. The model also showed no lack of fit at 95% level of significance. The ANOVA analysis for this model is shown in Table 2. The equation of the model based on the coded factors is given by the following equation:

$$\begin{aligned}\text{COD reduction }(\%) = 77.71 - 1.64A - 12.81B + 1.37C \\ - 2.42D + 4.14AB + 3.61BD - 7.77B^2 \\ - 11.12C^2 - 5.05D^2\end{aligned} \tag{5}$$

where A is the catalyst dosage (g L^{-1}), B paraquat concentration (mg L^{-1}), C pH and D the contact time (min) like parameters in photocatalytic degradation in Eq. 3. In this model, paraquat concentration and contact time were

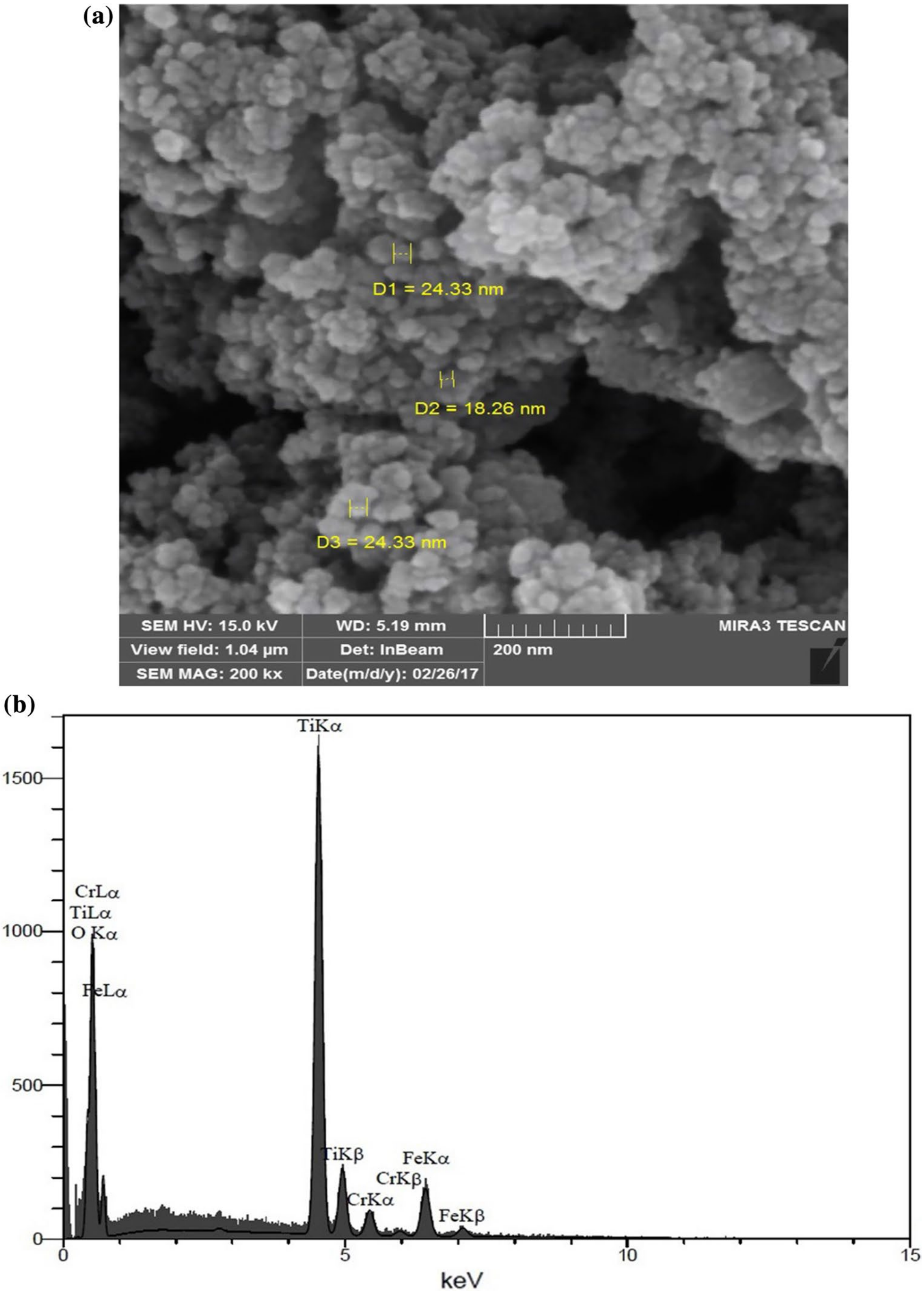

Fig. 4 **a** FESEM image for the α-Fe_2O_3@MIL-101(Cr)@TiO_2, **b** EDS spectrum of the α-Fe_2O_3@MIL-101(Cr)@TiO_2

determined as effective parameters on the COD reduction, while pH and catalyst dosage were not significant factors. In this case, B^2, C^2, D^2 and AB were also remarkable model terms.

Effect of parameters

The effect of catalyst dosage, paraquat concentration and their interactions on the photocatalytic degradation is shown in Fig. 5a under UV irradiation using the 3D response surface plot at pH 7 and contact time of 45 min (center point of the experimental design). The changing of catalyst dosage is an effective factor the photocatalytic degradation of paraquat (Nur-Afiqah et al. 2016). The percentage of photocatalytic degradation increased by enhancing catalyst amount up to 0.2 g L^{-1}, and then it decreased from 87.46 to 32.96% (Table 2: Exp. No 1,4). The major role for the improved photocatalytic elimination of paraquat is due to increase in the total active surface area of the catalyst. However, increasing the concentration of the catalyst above 0.4 g L^{-1} leads to decrease in degradation efficiency. The aggregation occurs at high concentrations of the optimum amount of the α-Fe_2O_3@MIL-101(Cr)@TiO_2 photocatalyst. As a result, the number of available paraquat molecules is not adequate to fill the active sites of the photocatalyst. Increased scattering and turbidity properties were observed in the high concentration of catalyst. So, the light does not penetrate all available surface of the catalyst. The aforementioned mechanism is the aggregation of α-Fe_2O_3@MIL-101(Cr)@TiO_2 at high concentration. This result was shown in previous studies on the degradation of herbicides (Mir et al. 2014; Mirmasoomi et al. 2016). So, maximum photocatalytic degradation was achieved 87.46% at pH 7 and contact time of 45 min with catalyst dosage 0.2 g L^{-1}. Removal of paraquat using the α-Fe_2O_3@MIL-101(Cr)@TiO_2 was studied by changing the initial concentration of paraquat (20–40 mg L^{-1}) with contact time (45 min) at pH 7. The percentage of photodegradation decreased from 87.46 to 29.45% with increasing the initial concentration of paraquat from 20 to 40 mg L^{-1} (Fig. 5b). Increasing the concentration of

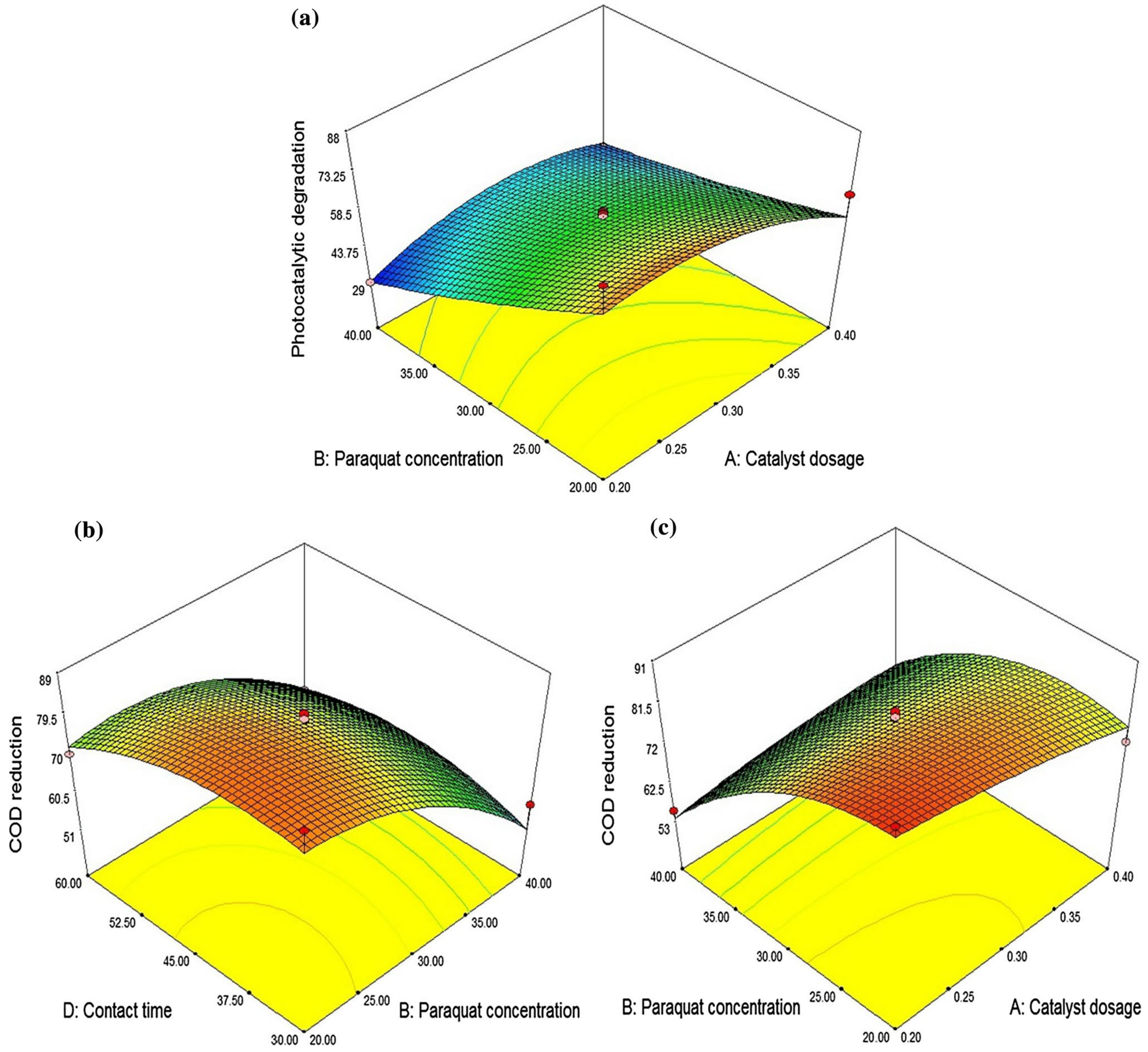

Fig. 5 Response surface plots showing the interaction between two parameters, **a** catalyst dosage and paraquat concentration, **b** contact time, time and paraquat concentration, **c** catalyst dosage and paraquat concentration

herbicide has inhibitive effect on the photocatalytic degradation. Adsorption sites on the photocatalyst are not enough for the adsorption of the all organic contaminants on the catalyst's surface (Nakaoka et al. 2010; Abramovic et al. 2013).

Figure 5b shows the effect of changing UV irradiation time and paraquat concentration on the COD reduction at pH 7 and catalyst dosage 0.3 g L^{-1}. The percentage of COD reduction decreased of (88.88 to 57.56%) with raising paraquat concentration of 20–40 mg L^{-1} at 30 min. The maximum COD reduction was detected 88.88% at pH 7 and 30 min with paraquat concentration 20 mg L^{-1}. Also, the percentage of COD reduction decreased from 88.88 to 53.32% with raising contact time from 45 to 60 min. The effect of varying catalyst dosage and paraquat concentration at pH 7 and contact time 45 min is shown in Fig. 5c. A significant decrease in COD removal is observed from 90.09 to 55.8% with increasing of paraquat concentration from 20 to 40 mg L^{-1}. Moreover, by raising catalyst dosage, COD reduction decreased from 90.09 to 72.69%. Decrease in removal efficiency is related to destabilization of the aggregated catalyst after the optimum contact time (Mir et al. 2014).

The comparison of photocatalytic degradation of paraquat in any process

The effect of catalyst and UV light was evaluated in the photocatalytic degradation of paraquat, as shown in Table 3. The different processes in removal efficiency of paraquat using UV-alone, UV/α-Fe_2O_3, UV/α-Fe_2O_3@MIL-101(Cr), UV/α-Fe_2O_3@MIL-101(Cr)@TiO_2 and α-Fe_2O_3@MIL-101(Cr)@TiO_2 in the absence of UV irradiation were compared in the same reaction conditions. These results are compared with the same studies on photodegradation of paraquat. The reactions were performed by 20 mg L^{-1} of paraquat, 0.2 g L^{-1} of catalyst and pH 7 at room temperature. The yield of photodegradation of paraquat in the absence of the α-Fe_2O_3@MIL-101(Cr)@TiO_2 catalyst was about 11.79%. The removal of paraquat was about 5% using a catalyst without UV radiation. The yield of the product under UV radiation was found to be 18.04 and 43.49% using the α-Fe_2O_3 and α-Fe_2O_3@MIL-101(Cr) catalyst after 45 min, respectively. It is observed that in the presence of both α-Fe_2O_3@MIL-101(Cr)@TiO_2 catalyst and UV light, 87.46% of the paraquat could be removed in 45 min. So, both of them are required for the effective degradation of paraquat. The photocatalytic degradation of organic material in solution is induced by the photoexcitation of the semiconductors such as TiO_2.

Optimum conditions

RSM can evaluate the optimum combination of factors using the optimization function to find the highest percentage of photocatalytic degradation and COD reduction. The maximum photocatalytic degradation and COD reduction were predicted 75.65 and 89.88%, respectively, under pH 7.10, catalyst dosage 0.2 g L^{-1}, paraquat concentration of 20 mg L^{-1} and 15 min. The actual experimental values achieved 87.56% for photocatalytic degradation with 4.3% deviation and 90.09% for COD reduction with 2.8% deviation.

Kinetics of paraquat adsorption on the surface of α-Fe_2O_3@MIL-101(Cr)@TiO_2

The kinetics of paraquat adsorption on the surface of α-Fe_2O_3@MIL-101(Cr)@TiO_2 in photocatalytic degradation and COD reduction were obtained by the experimental kinetic data. The kinetic models containing pseudo-first-order, pseudo-second-order, parabolic diffusion model and modified Freundlich model were used. Degradation of kinetic experiments was investigated at adsorbent dosage of 0.2 g L^{-1}, pH 7 and paraquat concentration of 20 mg L^{-1}.

Table 3 Comparison of photocatalytic degradation paraquat

Entry	Systems	Catalyst dosage (g L^{-1})	Paraquat concentration (mg L^{-1})	pH	Time (min)	Removal efficiency (%)	References
1	UV/TiO_2	0.2	40	6.6	180	100	Moctezuma et al. (1999)
2	Cu-UV/TiO_2/SBA-15	0.5	10	3	420	71	Sorolla et al. (2012)
3	UV/N, S-TiO_2 thin films	30.8	10	5.8	300	84.39	Zahedi et al. (2015)
4	UV/$ZrTiO_4$/$ZrTi_2O_6$/TiO_2	0.3	15	7	240	84.41	Nur-Afiqah et al. (2016)
5	UV/TiO_2	1.5	20	6	180	66	Nagaraju et al. (2017)
6	UV/α-Fe_2O_3	0.2	20	7	45	18.04	This work
7	UV/α-Fe_2O_3@MIL-101(Cr)	0.2	20	7	45	43.49	This work
8	UV/α-Fe_2O_3@MIL-101(Cr)@TiO_2	0.2	20	7	45	87.46	This work

Reaction condition: room temperature

Table 4 Kinetic parameters for photocatalytic degradation and COD reduction of paraquat using the initial concentrations = 20 mg L^{-1}, catalyst dosage = 0.2 g L^{-1} and pH 7

Entry	Degradation of paraquat	Pseudo-first order		Pseudo-second order		Parabolic diffusion		Modified Freundlich	
		k^1	R^2	K^2	R^2	k	R^2	k	R^2
1	Photocatalytic degradation	0.0126	0.8142	0.0053	0.9986	0.3379	0.9904	0.0389	0.9562
2	COD reduction	0.0574	0.9467	0.0082×10^{-3}	0.9931	0.2244	0.9891	0.2338	0.9401

The pseudo-first-order kinetic model is shown as follows (Langmuir 1918):

$$\mathrm{Ln}(q_e - q_t) = \mathrm{Ln}(q_e) - k_{1t} \tag{6}$$

In Eq. 6, k_1 is the equilibrium rate constant (min^{-1}), q_e and q_t are the amount of paraquat adsorbed at equilibrium (mg g^{-1}) and amount of paraquat adsorbed at any time t (mg g^{-1}) (Bulut et al. 2008).

The pseudo-second-order kinetic model is shown as follows (Ho and McKay 1998):

$$\frac{t}{q_t} = \frac{1}{k^2 q_e^2} + \left(\frac{1}{q_e}\right)t \tag{7}$$

In this Eq. 7, k_2 is the rate equilibrium rate constant (g mg^{-1} min^{-1}) (Ho and McKay 1998).

The parabolic diffusion model is used to explain diffusion-controlled phenomena in catalyst which can be stated as follows (Kodama et al. 2001):

$$\left(\frac{\left(1-\left(\frac{c_t}{c_0}\right)\right)}{t}\right) = kt^{-\frac{1}{2}} + \alpha \tag{8}$$

where k is the rate coefficient, C_0 and C_t are the concentration of paraquat (mg L^{-1}) at time 0 and time t, respectively, and a is a constant in Eq. 8.

The modified Freundlich model was applied to determine ion exchange or adsorption in soils and clays that is shown as follows (Kuo and Lotse 1974; Kodama et al. 2001):

$$\frac{C_o - C_t}{C_o} = kt^b \tag{9}$$

In Eq. 9, k is rate coefficient, C_0 and C_t are the concentration of paraquat (mg L^{-1}) at time 0 and time t, respectively, and b is a constant. The photocatalytic degradation and COD reduction of paraquat are evaluated by the pseudo-first-order, pseudo-second-order, parabolic diffusion and modified Freundlich kinetic parameters that are summarized in Table 4.

The kinetic data for photocatalytic degradation and COD reduction in paraquat fitted with the pseudo-second-order and parabolic diffusion models (Fig. 6). These models have a good result in fast degradation of paraquat at the short time according to the literature (Kumar et al. 2012). The pseudo-second-order model was adjusted to the data with an R^2 of 0.9986 for photocatalytic degradation and R^2 of 0.9931 for COD reduction, respectively. The rapid degradation of paraquat within a short time is due to a strong cation-exchange interaction between paraquat ion and the charged surface in the synthesized catalyst (Tsai and Chen 2013). The parabolic diffusion model was fitted to the data with an R^2 of 0.9904 for photocatalytic degradation and R^2 of 0.9891 for COD reduction, respectively. These results show that the electron transfer at the rate-limiting step can be controlled by diffusion of the paraquat molecules from solution to the active sites of the α-Fe_2O_3@MIL-101(Cr)@TiO_2 surface.

Conclusion

In this research, a novel magnetic α-Fe_2O_3@MIL-101(Cr)@TiO_2 photocatalyst was successfully synthesized. The structural and morphological properties of photocatalyst were studied by FTIR, XRD, SEM, EDX and BET analyses. Response surface methodology based on Box–Behnken design was effectively used to optimize the removal parameters. Also, the adsorption kinetics results were explained by the pseudo-second-order and parabolic diffusion models. The maximum photocatalytic degradation and COD reduction were achieved 87.46% and 90.09% at optimal conditions with paraquat concentration 20 mg L^{-1}, catalyst dosage 0.2 g L^{-1}, pH 7 and contact time 45 min. These results well matched with the predicted values in optimum conditions. So the synthesized photocatalyst is introduced as an excellent catalyst for the degradation paraquat.

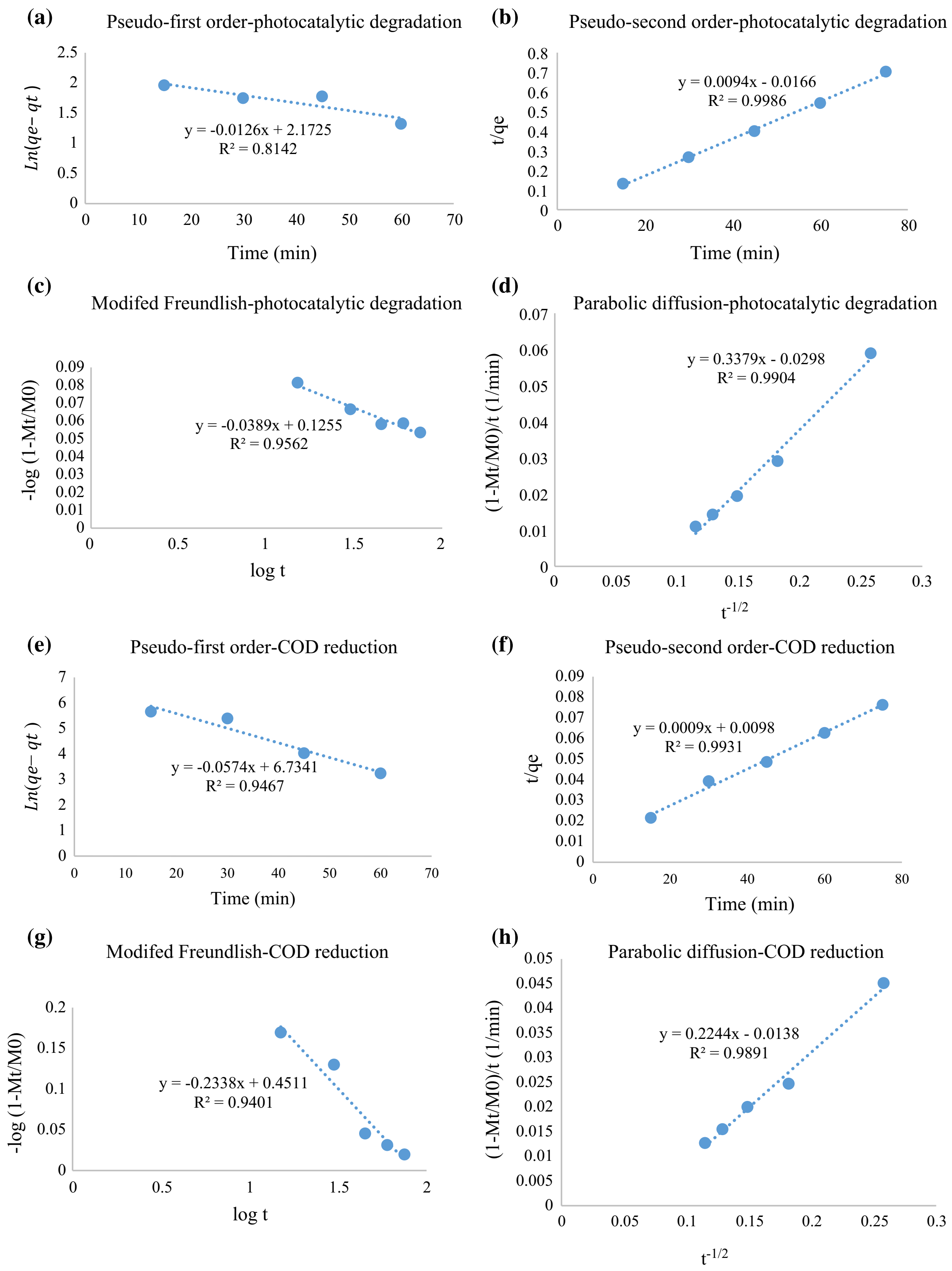

Fig. 6 Kinetic models of the photocatalytic degradation and COD reduction of paraquat (**a**), **e** pseudo-first-order, **b**, **f** pseudo-second-order, **c**, **g** modified Freundlich and **d**, **h** parabolic diffusion models

Acknowledgements We gratefully acknowledge the staffs of the Research Council of Islamic Azad University of Damavand for their collaboration in this study.

References

Abramovic BF, Despotovic VN, Sojic DV, Orcic DZ, Csanadi JJ, Cetojevic Simin DD (2013) Photocatalytic degradation of the herbicide clomazone in natural water using TiO_2: kinetics, mechanism, and toxicity of degradation products. Chemosphere 93:166–171. https://doi.org/10.1016/j.chemosphere.2013.05.024

Ahmed S, Rasul MG, Brown R, Hasib MA (2011) Influence of parameters on the heterogeneous photocatalytic degradation of pesticides and phenolic contaminants in wastewater: a short review. J Environ Manage 92:311–330. https://doi.org/10.1016/j.jenvman.2010.08.028

Alvarez A, Maria Saez J, Davila Costa J, Leticia Colin V, Maria Soledad Fuentes M, Sergio Antonio Cuozzo S, Susana Benimeli C, Marta Alejandra Polti M, Julia Amoroso M (2016) Actinobacteria: current research and perspectives for bioremediation of pesticides and heavy metals. Chemosphere 166:41–62. https://doi.org/10.1016/j.chemosphere.2016.09.070

American Public Health Association (APHA) (2005) Standard methods for the examination of water and wastewater, 21st edn. American Water Works Association, Water Environment Federation, Washington

Bajuk-Bogdanovic D, Jovic A, Vasiljevic BN, Milojevic-Rakica M, Kragovic M, Krajisnik D, Holclajtner-Antunovica I, Dondura V (2017) 12-Tungstophosphoric acid/BEA zeolite composites-characterization and application for pesticide removal. Mater Sci Technol B 225:60–67. https://doi.org/10.1016/j.mseb.2017.08.011

Beydoun D, Amal R, Low GKC, McEvoy S (2000) Novel photocatalyst: titania-coated magnetite. Activity and photodissolution. J Phys Chem B 104:4387–4396. https://doi.org/10.1021/jp992088c

Bhattacharjee S, Chena Ahn WS (2014) Chromium terephthalate metal–organic framework MIL-101: synthesis, functionalization, and applications for adsorption and catalysis. RSC Adv 4:52500–52525. https://doi.org/10.1039/C4RA11259H

Bulut E, Özacar M, Sengil IA (2008) Equilibrium and kinetic data and process design for adsorption of Congo Red onto bentonite. J Hazard Mater 154:613–622. https://doi.org/10.1016/j.jhazmat.2007.10.071

Castillo Diaz JM, Delgado-Moreno L, Nunez R, Nogales R, Romero E (2016) Enhancing pesticide degradation using indigenous microorganisms isolated under high pesticide load in bioremediation systems with vermicomposts. Bioresour Technol 214:234–241. https://doi.org/10.1016/j.biortech.2016.04.105

Chen X, Mao SS (2007) Titanium dioxide nanomaterials: synthesis, properties, modifications, and applications. Chem Rev 107:2891–2959. https://doi.org/10.1021/cr0500535

Chen JS, Chen CP, Liu J, Xu R, Qiao SZ, Lou XW (2011) Ellipsoidal hollow nanostructures assembled from anatase TiO_2 nanosheets as a magnetically separable photocatalyst. Chem Commun 47:2631–2633. https://doi.org/10.1039/C0CC04471G

Cheng P, Qiu J, Gu M, Shangguan W (2004) Synthesis of shape-controlled titania particles from a precursor solution containing urea. Mater Lett 58:3751–3755. https://doi.org/10.1016/j.matlet.2004.08.008

Corma A, Garcia H, Xamena FXL (2010) Engineering metal organic frameworks for heterogeneous catalysis. Chem Rev 110:4606–4655. https://doi.org/10.1021/cr9003924

Daneshvar N, Aber S, Seyed Dorraji MS, Khataee AR, Rasoulifard MH (2007) Photocatalytic degradation of the insecticide diazinon in the presence of prepared nanocrystalline ZnO powders under irradiation of UV-C light. Sep Purif Technol 58:91–98. https://doi.org/10.1016/j.seppur.2007.07.016

De-Almeida RM, Yonamine M (2007) Gas chromatographic-mass spectrometric method for the determination of the herbicides paraquat and diquat in plasma and urine samples. J Chromatogr B 853:260–264. https://doi.org/10.1016/j.jchromb.2007.03.026

Dekrafft KE, Wang C, Lin W (2012) Metal-organic framework templated synthesis of Fe_2O_3/TiO_2 nanocomposite for hydrogen production. Adv Mater 24:2014–2018. https://doi.org/10.1002/adma.201200330

Dhaouadi A, Adhoum N (2009) Degradation of paraquat herbicide by electrochemical advanced oxidation methods. J Electroanal Chem 637:33–42. https://doi.org/10.1016/j.jelechem.2009.09.027

Doulia DS, Anagnos EK, Liapis KS, Klimentzos DA (2016) Removal of pesticides from white and red wines by microfiltration. J Hazard Mater 317:135–146. https://doi.org/10.1016/j.jhazmat.2016.05.054

E-Shall MS, Abdelsayed V, Khder AERS, Hassan HMA, El-Kaderi HM, Reich TE (2009) Metallic and bimetallic nanocatalysts incorporated into highly porous coordination polymer MIL-101. J Mater Chem 19:7625–7631. https://doi.org/10.1039/B912012B

Florencio MH, Pires E, Castro AL, Nunes MR, Borges C, Costa FM (2004) Photodegradation of diquat and paraquat in aqueous solutions by titanium dioxide: evolution of degradation reactions and characterisation of intermediates. Chemosphere 55:345–355

Fu JF, Zhao YQ, Xue XD, Li WC, Babatunde AO (2009) Multivariate-parameter optimization of acid blue-7 wastewater treatment by Ti/TiO_2 photoelectrocatalysis via Box–Behnken design. Desalination 243:42–51. https://doi.org/10.1016/j.desal.2008.03.038

Gobas FPC, Zhang X, Wells R (1993) Gastrointestinal magnification: the mechanism of bio magnification and food chain accumulation of organic chemicals. Environ Sci Technol 27:2855–2863. https://doi.org/10.1021/es00049a028

Guo ZC, Shao CL, Zhang MY, Mu JB, Zhang ZY, Zhang P, Chen P, Liu YC (2011) Dandelion-like Fe_3O_4@CuTNPc hierarchical nanostructures as a magnetically separable visible-light photocatalyst. J Mater Chem 21:12083–12088. https://doi.org/10.1039/C1JM11098E

Ho YS, McKay GA (1998) Comparison of chemisorption kinetic models applied to pollutant removal on various sorbents. Process Saf Environ Prot 76(4):332–340. https://doi.org/10.1205/095758298529696

Horcajada P, Serre C, Maurin G, Ramashye NA, Balas F, Vallet-Regi M, Sebban M, Taulelle F, Ferey G (2008) Flexible porous metal-organic frameworks for a controlled drug delivery. J Am Chem Soc 130:6774–6780. https://doi.org/10.1021/ja710973k

Horcajada P, Chalati T, Serre C, Gillet B, Sebrie C, Baati T, Eubank JF, Heurtaux D, Clayette P, Kreuz C, Chang JS, Hwang YK, Marsaud V, Bories PN, Cynober L, Gil S, Ferey G, Couvreur P, Gref R (2011) Porous metal-organic-framework nanoscale carriers as a potential platform for drug delivery and imaging. Nat Mater 9:172–178. https://doi.org/10.1038/nmat2608

Horwitz W (2000) Standard methods for the examination of water and wastewater, 20th edn. APHA, Washington

Jhung SH, Lee JH, Yoon JW, Serre C, Ferey G, Chang JS (2007) Microwave synthesis of chromium terephthalate MIL-101 and its benzene sorption ability. Adv Mater 19(1):121–124. https://doi.org/10.1002/adma.200601604

Kang M (2002) Preparation of TiO_2 photocatalyst film and its catalytic performance for 1,1-dimethyl-4,4-bipyidium dichloride decomposition. Appl Catal B Environ 37:187–196. https://doi.org/10.1016/S0926-3373(01)00303-4

Kearney PC, Ruth JM, Zeng Q, Mazzocchi P (1985) UV-ozonation of paraquat. J Agric Food Chem 33:953–957. https://doi.org/10.1021/jf00065a044

Kida M, Ziembowicz S, Koszelnik P (2018) Removal of organochlorine pesticides (OCPs) from aqueous solutions using hydrogen peroxide, ultrasonic waves, and a hybrid process. Sep Purif Technol 192:457–464. https://doi.org/10.1016/j.seppur.2017.10.046

Kodama T, Harada Y, Ueda M, Shimizu K, Shuto K, Komarneni S (2001) Selective exchange and fixation of strontium ions with ultrafine Na-4-mica. Langmuir 17:4881–4886. https://doi.org/10.1021/la001774w

Kown YT, Song KY, Lee WI, Choi GJ, Do YR (2000) Photochemistry behavior of WO_3-loaded TiO_2 in an oxidation reaction. J Catal 191:192–199. https://doi.org/10.1006/jcat.1999.2776

Kumar R, Jain SK, Misra RK, Kachchwaha M, Khatri PK (2012) Aqueous heavy metals removal by adsorption on β-diketone-functionalized styrene–divinylbenzene copolymeric resin. Int J Environ Sci Technol 9:79–84. https://doi.org/10.1007/s13762-011-0019-1

Kuo S, Lotse G (1974) Kinetics of phosphate adsorption and desorption by hematite and gibbsite1. Soil Sci 116:400–406. https://doi.org/10.1097/00010694-197312000-00002

Langmuir I (1918) The adsorption of gases on plane surfaces of glass, mica and platinum. J Am Chem Soc 40(9):1361–1403. https://doi.org/10.1021/ja02242a004

Lee S, Drwiega J, Wu CY, Mazyck D, Sigmund WM (2004) Anatase TiO_2 nanoparticle coating on barium ferrite using titanium bis-ammonium lactato dihydroxide and its use as a magnetic photocatalyst. Chem Mater 16:1160–1164. https://doi.org/10.1021/cm0351902

Lei L, Chu HP, Hu X, Yue PL (1999) Preparation of heterogeneous photocatalyst (TiO_2/alumina) by metallo-organic chemical vapor deposition. Ind Eng Chem Res 38:3381–3385. https://doi.org/10.1021/ie980677j

Li JR, Kuppler RJ, Zhou HC (2009) Selective gas adsorption and separation in metal-organic frameworks. Chem Soc Rev 38:1477–1504. https://doi.org/10.1039/B802426J

Lin H, Liao S, Hung S (2005) The dc thermal plasma synthesis of ZnO nanoparticles for visible-light photocatalyst. J Photochem Photobiol A Chem 174:82–87. https://doi.org/10.1016/j.jphotochem.2005.02.015

Liu B, Torimoto T, Yoneyama H (1998) Photocatalytic reduction of CO_2 using surface-modified CdS photocatalysts in organic solvent. J Photochem Photobiol A Chem 113:93–97. https://doi.org/10.1016/S1010-6030(97)00318-3

Liu G, Li L, Xu D, Huang X, Xu X, Zheng S, Zhang Y, Lin H (2017) Metal-organic framework preparation using magnetic graphene oxide-β-cyclodextrin for neonicotinoid pesticide adsorption and removal. Carbohydr Polym 175:584–591. https://doi.org/10.1016/j.carbpol.2017.06.074

Makovec D, Sajko M, Selisnik A, Drofenik M (2011) Magnetically recoverable photocatalytic nanocomposite particles for water treatment. Macromol Chem Phys 129:83–94. https://doi.org/10.1016/j.matchemphys.2011.03.059

Maksimchuk NV, Timofeeva MN, Melgunov MS, Shmakov AN, Chesalov YA, Dybtsev DN, Fedin VP, Kholdeeva OA (2008) Heterogeneous selective oxidation catalysts based on coordination polymer MIL-101 and transition metal-substituted polyoxometalates. J Catal 257(2):315–323. https://doi.org/10.1016/j.jcat.2008.05.014

Marien CBD, Cottineau T, Robert D, Drogui P (2016) TiO_2 nanotube arrays: influence of tube length on the photocatalytic degradation of paraquat. Appl Catal B Environ 194:1–6. https://doi.org/10.1016/j.apcatb.2016.04.040

Mir NA, Haque M, Khan A, Muneer M, Vijayalakshmi S (2014) Photocatalytic degradation of herbicide Bentazone in aqueous suspension of TiO_2: mineralization, identification of intermediates and reaction pathways. Environ Technol 35:407–415. https://doi.org/10.1080/09593330.2013.829872

Mirmasoomi SR, Mehdipour Ghazi M, Galedari M (2016) Photocatalytic degradation of diazinon under visible light using TiO_2/Fe_2O_3 nanocomposite synthesized by ultrasonic-assisted impregnation method. Sep Purif Technol 175:418–427. https://doi.org/10.1016/j.seppur.2016.11.021

Moctezuma E, Leyva E, Monreal E, Villegas N, Infante D (1999) Photocatalytic degradation of the herbicide “Paraquat”. Chemosphere 39(3):511–517. https://doi.org/10.1016/S0045-6535(98)00599-2

Nagaraju P, Khunphonoi R, Harikaranahalli Puttaiah S, Suwannaruang T, Kaewbuddee C, Wantala K (2017) Photocatalytic paraquat degradation over TiO_2 modified by hydrothermal technique in alkaline solution. J Adv Oxid Technol 20:1–12. https://doi.org/10.1515/jaots-2017-0004

Nakaoka Y, Katsumata H, Kaneco S, Suzuki T, Ohta K (2010) Photocatalytic degradation of diazinon in aqueous solution by platinized TiO_2. Desalin Water Treat 13:427–436. https://doi.org/10.5004/dwt.2010.1000

Nguyen HTT, Doan DNA, Truong T (2017) Unprecedented salt-promoted direct arylation of acidic sp2 CH bonds under heterogeneous Ni-MOF-74 catalysis: synthesis of bioactive azole derivatives. J Mol Catal A: Chem 426:141–149. https://doi.org/10.1016/j.molcata.2016.11.009

Noguchi T, Fujishima A, Sawunyama P, Hashimoto K (1998) Photocatalytic degradation of gaseous formaldehyde using TiO_2 film. Ind Eng Chem Res 32:3831–3833. https://doi.org/10.1021/es980299

Nur-Afiqah B, Rusmidah A, Wan Azelee Wan AB, Leny Y (2016) Role of heterojunction $ZrTiO_4$/$ZrTi_2O_6$/TiO_2 photocatalyst towards the degradation of paraquat dichloride and optimization study by Box–Behnken design. Arab J Chem. https://doi.org/10.1016/j.arabjc.2016.02.011

Petit V, Cabridenc R, Swannell RPJ, Sokhi RS (1995) Review strategies for modelling the environmental fate of pesticides discharged into riverine systems. Environ Int 21(2):167–176. https://doi.org/10.1016/0160-4120(95)00006-2

Plakas KV, Karabelas AJ (2012) Removal of pesticides from water by NF and RO membranes—a review. Desalination 287:255–265. https://doi.org/10.1016/j.desal.2011.08.003

Real FJ, Benitez FJ, Acero JL, Gonzalez M (2007) Removal of diazinon by various advanced oxidation processes. J Chem Technol Biotechnol 82:566–574. https://doi.org/10.1002/jctb.1702

Reddy PVL, Kim KH (2015) A review of photochemical approaches for the treatment of a wide range of pesticides. J Hazard Mater 285:325–335. https://doi.org/10.1016/j.jhazmat.2014.11.036

Roy P, Berger S, Schmuki P (2011) TiO_2 nanotubes: synthesis and applications. Angew Chem Int Ed 50:2904–2939. https://doi.org/10.1002/anie.201001374

Saini R, Kumar P (2016) Simultaneous removal of methyl parathion and chlorpyrifos pesticides from model wastewater using coagulation/flocculation: central composite design. J Environ Chem 4(1):673–680. https://doi.org/10.1016/j.jece.2015.12.020

Sajjadifar S, Abbasi Z, Rezaee Nezhad E, Rahimi Moghaddam M, Karimian S, Miri S (2014) Ni^{2+} supported on hydroxyapatite-core-shell γ-Fe_2O_3 nanoparticles: a novel, highly efficient and reusable Lewis acid catalyst for the regioselective azidolysis of epoxides in water. J Iran Chem Soc 11(2):335–340. https://doi.org/10.1007/s13738-013-0304-7

Shabeer TP, Saha A, Gajbhiye VT, Gupta S, Manjaiah KM, Varghese E (2014) Simultaneous removal of multiple pesticides from water: effect of organically modified clays as coagulant aid and adsorbent in coagulation-flocculation process. Environ Technol 35:2619–2627. https://doi.org/10.1080/09593330.2014.914573

Sorolla MG, Dalida ML, Khemthong P, Grisdanurak N (2012) Photocatalytic degradation of paraquat using nano-sized Cu-TiO_2/SBA-15 under UV and visible light. J Environ Sci 24(6):1125–1132. https://doi.org/10.1016/S1001-0742(11)60874-7

Su H, Lin Y, Wang Z, Wong YL, Chen X, Chen TW (2016) Dominic Chan, Magnetic metal-organic framework-titanium dioxide nanocomposite as adsorbent in the magnetic solid-phase extraction of fungicides from environmental water samples. J Chromatogr A 1466:21–28. https://doi.org/10.1016/j.chroma.2016.08.066

Taylor-Pashow KML, Rocca JD, Xie ZG, Tran S, Lin WB (2009) Post-synthetic modifications of iron-carboxylate nanoscale metal-organic frameworks for imaging and drug delivery. J Am Chem Ceram Soc 131(40):14261–14263. https://doi.org/10.1021/ja906198y

Tennakone K, Kottegoda IRM (1996) Photocatalytic mineralization of paraquat dissolved in water by TiO_2 supported on polythene and polypropylene films. J Photochem Photobiol A Chem 93:79–81. https://doi.org/10.1016/1010-6030(95)04141-9

Trovo AG, Gomes Junior O, Machado AEH, Borges Neto W, Silva JO (2013) Degradation of the herbicide paraquat by photo-Fenton process: optimization by experimental design and toxicity assessment. J Braz Chem Soc 24(1):76–84. https://doi.org/10.1590/S0103-50532013000100011

Tsai WT, Chen HR (2013) Adsorption kinetics of herbicide paraquat in aqueous solution onto a low-cost adsorbent, swine-manure-derived biochar. Int J Environ Sci Technol 10(6):1349–1356. https://doi.org/10.1007/s13762-012-0174-z

Wang Y, Li SK, Xing XR, Huang FZ, Shen YH, Xie AJ, Wang XF, Zhang J (2011) Self-Assembled 3D flowerlike hierarchical Fe_3O_4@Bi_2O_3 core–shell architectures and their enhanced photocatalytic activity under visible light. Chem Eur J 17:4802–4808. https://doi.org/10.1002/chem.201001846

Wee LH, Bonino F, Lamberti C, Bordigab S, Martensa JA (2014) Cr-MIL-101 encapsulated Keggin phosphotungstic acid as active nanomaterial for catalysing the alcoholysis of styrene oxide. Green Chem 16:1351–1357. https://doi.org/10.1039/C3GC41988F

Xi GC, Yue B, Cao JY, Ye JH (2011) Fe_3O_4/WO_3 hierarchical core–shell structure: high-performance and recyclable visible-light photocatalysis. Chem Eur J 17:5145–5154. https://doi.org/10.1002/chem.201002229

Xu Y, Chen Q, Yang H, Lv M, He Q, Liu X, Wei F (2015) Enhanced photodegradation of Rhodamine B under visible light by N-$K_2Ti_4O_9$/MIL-101. Compos Mater Sci Semicond Process 36:115–119. https://doi.org/10.1016/j.mssp.2015.03.025

Zahedi F, Behpour M, Ghoreishi SM, Khalilian H (2015) Photocatalytic degradation of paraquat herbicide in the presence TiO_2 nanostructure thin films under visible and sun light irradiation using continuous flow photoreactor. Sol Energy 120:287–295. https://doi.org/10.1016/j.solener.2015.07.010

Zhang Y, Zhang W, Liao X, Zhang J, Hou Y, Xiao Z, Chen F, Hu X (2010) Degradation of diazinon in apple juice by ultrasonic treatment. Ultrason Sonochem 17(4):662–668. https://doi.org/10.1016/j.ultsonch.2009.11.007

Zhao D, Timmons DJ, Yuan D, Zhou HC (2011) Tuning the topology and functionality of metal-organic frameworks by ligand design. Acc Chem Res 44:123–133. https://doi.org/10.1021/ar100112y